Smart Structures and Systems, *Vol. 34, No. 5 (2024) 311-322*
https://doi.org/10.12989/sss.2024.34.5.311

Bayesian compressed sensing-based tomographic method for corrosion monitoring

Zengnian Xin*[1] and Ming Chang [2a]

[1] *Research Center of Structural Health Monitoring and Prognosis, State Key Laboratory of Mechanics and Control for Aerospace Structures, Nanjing University of Aeronautics and Astronautics, 29 Yudao Street, Nanjing, Republic of China*
[2] *School of Electrical, Energy and Power Engineering, Yangzhou University, 88 South University Road, Yangzhou, Republic of China*

(*Received October 18, 2024, Revised December 4, 2024, Accepted December 11, 2024*)

Abstract. For airplanes, especially aging airplanes, corrosion is widespread. As the corrosion reaches a certain level, it may cause flight accidents. Lamb wave tomography (LWT), as one of the Structural Health Monitoring technologies, can be used to monitor the corrosion of aircraft structures. However, the LWT requires densely arranged sensors on both sides of the monitoring area and has the poor imaging quality. These disadvantages limit its application in aircraft corrosion monitoring. In view of this situation, this paper proposes Bayesian Compressed Sensing (BCS)-based tomographic method to monitor corrosion of aircraft structure. BCS-based tomographic method reduces the number of sensors by under-sampling the received lamb wave signal and utilizes a Bayesian formulation to perform the original signal reconstruction. Compared to conventional LWT, the new method has better imaging quality with fewer sensors. Compared to the improved Compressed Sensing (CS)-based tomographic, BCS-based tomographic has fewer imaging artifacts, and shorter imaging time. Simulation and experiment are carried out on aviation aluminum plate with corrosion to verify the new proposed method. The results show the advantages of the proposed BCS-based tomographic method.

Keywords: aircraft structure; Bayesian Compressed Sensing; corrosion monitoring; lamb wave tomography

1. Introduction

Corrosion is one of the main causes of damage to the structural surface. For airplanes, especially aging airplanes, due to the influence of the flight environment, are vulnerable to corrosion (Braga *et al*. 2014). As the corrosion damage reaches a certain level, it may cause serious flight accidents and endanger the personnel on board (Alexopoulos *et al*. 2012).

For the early corrosion damage of aircraft structure, it has the characteristics of small area and strong concealment. Traditional visual method and non-destructive testing method is hard to carry out the effective monitoring. The structural health monitoring (SHM) technology based on lamb waves uses piezoelectric (PZT) sensors deployed on the structural surface to excite and receive Lamb wave in the structure, then by analyzing the Lamb wave response signal in the non-damage state and the lamb wave response signal after damage occurs, the small damage in a certain area of aircraft structure can be monitored and the damage degree can be evaluated (Vivar-Perez *et al*. 2014, Garg *et al*. 2016, Gorgin and Wang 2021). Therefore, in recent years, more and more researchers have applied it to corrosion monitoring of structures (Bao *et al*. 2019, Cirtautas *et al*. 2022, Livadiotis *et al*. 2023, Zima *et al*. 2022, Huang *et al*. 2024).

Lamb wave tomography (LWT) is an important imaging method of SHM based on lamb wave. It scans the monitored area in different directions by exciting the lamb wave to obtain the changes in acoustic parameters during the propagation process, thereby realizing the monitoring of the damage inside the structure. As long as enough sensors are arranged around the monitoring area, almost all damage scattering information can be collected, and then the LWT method can be used to obtain high precision diagnostic images (Huang *et al*. 2016). According to the arrangement of sensors, LWT can be divided into cross-hole LWT, fan beam LWT and double cross-hole LWT. Zhao *et al*. (2011) studied the ray distribution of LWT, and compared the imaging effects of the three kinds of LWT. The results show that cross-hole LWT has the lowest imaging accuracy, but requires the least number of sensors; double cross-hole LWT has highest imaging accuracy and requires a large number of sensors, both the imaging effect and the number of sensors of fan beam LWT are somewhere in between. In addition, reconstruction algorithm also has a great impact on imaging quality. There are many image reconstruction algorithms in LWT, and the most used in structural health monitoring are Filtered Back Projection (FBP), Algebraic Reconstruction Technique (ART), and Simultaneous Iterative Reconstruction Technique (SIRT). Among the three algorithms, SIRT is an iterative algorithm, and its iterative process is to updates each pixel value by correcting all projection lines, so it has better imaging effect than others (Belanger 2010). In view of the above

*Corresponding author, Ph.D. Student,
E-mail: xizengnian@nuaa.edu.cn
[a] Ph.D.

ISSN: 1738-1584 (Print), 1738-1991 (Online)

considerations, the LWT sensor layout adopts the cross-hole architecture, and the reconstruction algorithm uses the SIRT reconstruction method to monitor the corrosion in this article.

However, in order to obtain better imaging result, LWT is necessary to arrange dense sensors around the monitoring area to generate enough scanning rays. Meanwhile, SIRT iteration needs to calculate the weighted average, which makes the calculation complicated and slow. Aircraft structure corrosion monitoring system requires small weight and fast imaging speed to achieve real-time monitoring. These shortcomings limit the application of LWT in aircraft structure corrosion monitoring.

Compressed sensing (CS) theory represent that as long as the signal is sparse or compressible, the sparse high dimensional signal can be sampled by a sampling matrix into low dimensional signal, then by solving the optimization problem, the original signal can be reconstructed with high probability from this low dimensional signal (Donoho 2006, Tsaig and Donoho 2006, Candes *et al*. 2006). Using CS theory, the amount of data collected by the sensors can be reduced, and the goal of simplifying the system can be achieved. To simplify LWT, Chang *et al*. (2020) proposed CS-based tomography method to monitor the corrosion of aircraft structure by using a reduced number of sensors. The experimental result shows that the CS-based tomography method can accurately reconstruct the corrosion position with a smaller number of sensors. However, the imaging by CS-based tomography method has many artifacts in the presence of noise, and even if the imaging speed is faster than LWT, it is still slower, which affects real-time imaging. Therefore, it is necessary to further improve the CS-based tomographic method.

Ji *et al*. (2008) introduced the relevant ideas of Bayesian estimation into the CS reconstruction and proposed Bayesian Compressed Sensing (BCS). BCS provides a posterior density function of parameters to replace the point estimation of the parameters, which can provide sparser images than CS. And Bayesian takes into account Gaussian noise encountered in the compression sampling process, so it has better denoising performance (Xu *et al*. 2012). Due to these advantages of BCS, it has been gradually used in various fields in recent years (He *et al*. 2023, Kullaa 2021, Salucci *et al*. 2022, Xiao *et al*. 2024). In order to further improve the imaging quality in noisy environment, while shorten the imaging time, BCS-based tomographic method for corrosion monitoring of aircraft structures is proposed in this paper. Simulation and experiment were carried out in an aluminum plate, results show that BCS-based tomography has obvious advantages.

In section 2, we introduce the traditional LWT imaging method. In section 3, the BCS theory is introduced. In section 4, BCS-based tomographic method is proposed. In section 5, we perform numerical simulation to verify the new BCS-based tomographic method in theoretically. In section 6, experiments are carried out to verify the new method, and the imaging effect were compared with traditional LWT and CS-based tomography. In section 7 conclusions are made.

2. Lamb wave tomography

When lamb wave propagates in metal plate, the wave velocity will change as the product of the frequency and the plate thickness changes. If the frequency of lamb wave remains unchanged, the variation of wave velocity is only related to the plate thickness. When the metal plate is subjected to corrosion and the structure becomes thin, the change of lamb wave velocity will cause the change of wave arrival time on the propagation path. From the arrival time of lamb wave, we can infer the velocity distribution of the measured area, and thus determine the location of the corrosion. That is the principle of lamb wave tomography.

In order to perform damage monitoring by LWT, the monitoring area is discretized and divided into N isometric grids. Sensors are arranged on both sides of the monitoring area in cross-hole manner, sensors on one side excite lamb wave and sensors on the other side receive the lamb wave. The lamb waves from excitation sensors scan the entire area, and generate M scan paths. Fig. 1 shows the layout of sensors and one of the paths. Here, l_{ij} represents the length of the i-th path in the j-th grid. $s_j = 1/v_j$, s_j is the reciprocal of the velocity of the j-th grid, called slowness. The propagation time of the lamb wave on the i-th scan path can be determined by Eq. (1)

$$t_i = \sum_{j=1}^{N} l_{ij} s_j \quad (i = 1, \ldots M) \tag{1}$$

Write the expression for lamb wave arrival time of all rays, as shown in Eq. (2)

$$T = LS \tag{2}$$

In Eq. (2), $\boldsymbol{T}$ represents lamb waves propagation time of M rays, which is an $M\times1$ dimensional vector. $\boldsymbol{S}$ represents the slowness of the lamb wave in all grids, which is an $N\times1$ dimensional vector. $\boldsymbol{L}$ is composed of l_{ij}, called the distance matrix, is an $M\times N$ dimensional matrix, each row represents a ray path, and each column represents a grid. For example, the l_{11} represents the intercept of the first ray path in the first grid, l_{11} represents the intercept of the first ray path in the second grid, and so on, the distance matrix $\boldsymbol{L}$ is described by Eq. (3)

$$\boldsymbol{L} = \begin{bmatrix} l_{11} & l_{12} & \cdots & l_{1N-1} & l_{1N} \\ \vdots & \vdots & \cdots & \vdots & \vdots \\ l_{M1} & l_{M2} & \cdots & l_{MN-1} & l_{MN} \end{bmatrix}_{M\times N} \tag{3}$$

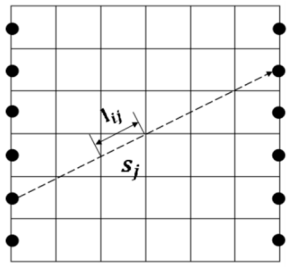

Fig. 1 Cross-hole arrangement of sensors

Assuming that the lamb wave slowness vector is $\boldsymbol{S}_0$ and the travel time vector is $\boldsymbol{T}_0$ when the measured structure is initially undamaged. And the actual measured signal slowness vector is $\boldsymbol{S}_1$ and the travel time vector is $\boldsymbol{T}_1$. Those parameters in the two states are put into Eq. (2), and we subtract the two newly obtained equations to obtain the time difference $\Delta\boldsymbol{T}$

$$\left.\begin{matrix}\boldsymbol{T_0} = \boldsymbol{LS_0} \\ \boldsymbol{T}_1 = \boldsymbol{LS}_1\end{matrix}\right\} \Rightarrow \boldsymbol{\Delta T} = \boldsymbol{L\Delta S} \tag{4}$$

Or

$$\begin{bmatrix}\Delta t_1 \\ \vdots \\ \Delta t_M\end{bmatrix} = \begin{bmatrix}l_{11} & \cdot & \cdot & \cdot & l_{1N} \\ \vdots & \cdot & \cdot & \cdot & \vdots \\ l_{M1} & \cdot & \cdot & \cdot & l_{MN}\end{bmatrix} \bullet \begin{bmatrix}\Delta s_1 \\ \cdot \\ \cdot \\ \cdot \\ \Delta s_N\end{bmatrix} \tag{5}$$

If corrosion occurs, the slowness value in the corresponding grid unit will change, that is to say, the slowness difference value in these grids is not zero. The lamb wave velocity of other grids without damage remains unchanged, so the remaining slowness difference value is zero. According to the lamb wave travel time difference before and after structural damage, LWT method calculates the slowness difference using Eq. (4). Then the slowness difference $\Delta\boldsymbol{S}$ is used as pixel imaging to highlight the corrosion damage in the measured area

LWT derives the slowness difference vector $\Delta\boldsymbol{S}$ through the distance matrix $\boldsymbol{L}$ and the travel time difference $\Delta\boldsymbol{T}$. Since the selection number of the sensor and the grid division of the measured area depend on the specific situation, the number of ray paths M and the number of unit grid N are generally different, usually M << N. In Eq. (5), the number of ray paths determines the number of equations, and the number of grids determines the number of unknows. In order to obtain an accurate solution, the number of equations M needs to be as large as possible. That is, the LWT method required densely arranged sensors, which increases the burden of the monitoring system and is limited in practical engineering applications.

In order to solve this problem, Chang *et al*. (2020) proposed CS-based tomographic method, which uses a sampling matrix to partially sample the lamb wave ray paths, and restores the slowness difference $\Delta\boldsymbol{S}$ from a small amount of wave arrival time difference $\Delta\boldsymbol{T}$ through CS reconstruction algorithm. This method reduces the number of sensors while enhancing imaging accuracy. The purpose of optimizing LWT can be achieved. However, in noisy environments, especially in the case of low Signal-to-Noise Ratio (SNR), the imaging effect of the CS-based tomography is not good, which has artifacts. And although the imaging time of the method is faster than that of LWT method, it is not fast enough for on-line monitoring. Therefore, it is necessary to further improve the existing CS-based tomography method, reduce the imaging time and enhance the imaging effect at low SNR.

3. Bayesian compressed sensing theory

3.1 Mathematical model of CS

Given an N×1 dimensional real signal $\boldsymbol{X}$, $\boldsymbol{X}\in\boldsymbol{R}^N$, it can be expanded into the following form under the N×N dimensional orthonormal basis $\boldsymbol{\Psi}$

$$x_i = \sum_{i=1}^{N} \alpha_i \psi_i \tag{6}$$

Or matrix form

$$\boldsymbol{X} = \boldsymbol{\Psi\alpha} \tag{7}$$

In Eq. (7), $\boldsymbol{\alpha}$ is the decomposition coefficient of $\boldsymbol{X}$, and it is an N×1 dimensional vector. If the number of non-zero elements in $\boldsymbol{\alpha}$ is K and $K << N$, then $\boldsymbol{\alpha}$ is said to K sparse. And $\boldsymbol{X}$ is a compressible signal. Then we can construct another $M \times N$ dimensional ($M < N$) measurement matrix $\boldsymbol{\Phi}$ that is not related to $\boldsymbol{\Psi}$, and perform a compressed observation on the signal $\boldsymbol{X}$ to obtain

$$\boldsymbol{y} = \boldsymbol{\Phi X} \tag{8}$$

$\boldsymbol{y}$ is an $M \times 1$ dimensional vector, and it is the linear observation (or projection) value of the original signal $\boldsymbol{X}$. Substituting Eq. (7) into Eq. (8), we get

$$\boldsymbol{y}_{M\times1} = \boldsymbol{\Phi}_{M\times N}\boldsymbol{X}_{N\times1} = \boldsymbol{\Phi}_{M\times N}\boldsymbol{\Psi}_{N\times N}\boldsymbol{\alpha}_{N\times1} = \boldsymbol{\Theta}_{M\times N}\boldsymbol{\alpha}_{N\times1} \tag{9}$$

Where $\boldsymbol{\Theta}$ is the observation matrix. Eq. (9) completes the compressed sampling from high-dimensional vector $\boldsymbol{\alpha}$ to low-dimensional vector $\boldsymbol{y}$.

3.2 Measurement matrix in CS

The purpose of measurement matrix $\boldsymbol{\Phi}$ is to obtain as few observations as possible while ensuring the accuracy of the reconstructed signal. The dimension of the measurement matrix directly determines the compressed sampling degree of the signal, and it is a bridge connecting the original signal and the measured signal. In order to ensure that the sampled signal can maintain the entire information of original signal, the measurement matrix must meet the Restricted Isometry Property (RIP) condition (Candes *et al*. 2006). That is, the RIP parameter δ_k of the measurement matrix $\boldsymbol{\Phi}$ is the minimum value δ that satisfies the following formula

$$(1-\delta)\|\boldsymbol{x}\|_2^2 \le \|\boldsymbol{\Phi x}\|_2^2 \le (1+\delta)\|\boldsymbol{x}\|_2^2 \tag{10}$$

However, it is difficult to calculate whether a given measurement matrix has RIP properties. In order to reduce the complexity of the problem, Baraniuk (2007) proposed a coherence discrimination theory, which shows that if it is guaranteed that the measurement matrix $\boldsymbol{\Phi}$ is not coherent with the spare basis $\boldsymbol{\Psi}$, the measurement matrix $\boldsymbol{\Phi}$ satisfies the RIP property with a high probability. In the application of CS, the independent and identically distributed Bernoulli matrix has little correlation with any sparse basis, and it is commonly used as a measurement matrix.

3.3 Reconstruction algorithm

In practical applications, $\boldsymbol{y}$ as an observation signal, is usually noisy, so equation (9) can be written as

$$\boldsymbol{y} = \boldsymbol{\Theta\alpha} + \boldsymbol{e} \tag{11}$$

Conventional CS reconstruction algorithm uses convex optimization problem with constraints to solve signal $\boldsymbol{\alpha}$, the expression is

$$\min_{\alpha} \|\boldsymbol{a}\|_1 \quad \boldsymbol{s.t.} \quad \|\boldsymbol{y} - \boldsymbol{\Theta a}\|_2 \leq \varepsilon \tag{12}$$

Where ε is an estimate of the noise in the original signal and $\varepsilon \geq 0$.

Unlike conventional CS reconstruction algorithm that uses Eq. (12) for point estimation of $\boldsymbol{\alpha}$, BCS uses Bayesian estimation to estimate the probability of signal $\boldsymbol{\alpha}$ in Eq. (11).

BCS algorithm assuming that the noise $\boldsymbol{e}$ in Eq. (11) is a Gaussian noise with a mean value of zero and a variance of σ_n^2. According to the knowledge of probability theory, the probability density function of $\boldsymbol{y}$ can be obtained as

$$p(\mathbf{y}|\boldsymbol{\alpha}, \sigma_n^2) = (2\pi\sigma_n^2)^{-\frac{M}{2}} \exp\left(-\frac{1}{2\sigma_n^2}\|\mathbf{y} - \boldsymbol{\Theta\alpha}\|^2\right) \tag{13}$$

In Eq. (13), the observation matrix $\boldsymbol{\Theta}$ and the measured value $\boldsymbol{y}$ are known, and the noise variance σ_n^2 is unknown, the problem is to estimate the signal $\boldsymbol{\alpha}$.

BCS solves the posterior probability distribution of signal $\boldsymbol{\alpha}$ by reasonably setting the prior distribution of sparse signal $\boldsymbol{\alpha}$.

The setting of the prior distribution directly determines the algorithm complexity and the accuracy of the estimation value $\hat{\boldsymbol{\alpha}}$. Ji *et al*. (2008) proposes that a hierarchical prior is applicable to BCS. It assumes that each element α_i in $\boldsymbol{\alpha}$ obeys a Gaussian prior distribution with a mean value of zero and a variance of σ_i^{-1}, namely

$$p(\boldsymbol{\alpha}|\boldsymbol{\sigma}) = \prod_{i=1}^{N} N(\alpha_i|0, \sigma_i^{-1}) \tag{14}$$

Assume that the inverse variance vector $\boldsymbol{\sigma}$ obeys the Gamma distribution with parameters a and b, namely

$$p(\boldsymbol{\sigma}|a, b) = \prod_{i=1}^{N} \Gamma(\sigma_i|a, b) \tag{15}$$

Substituting Eq. (15) into (14), the posterior probability density function of $\boldsymbol{\alpha}$ is

$$p(\boldsymbol{\alpha}|a, b) = \prod_{i=1}^{N} \int_0^{\infty} N(\alpha_i|0, \sigma_i^{-1})\, \Gamma(\sigma_i|a, b) d\sigma_i \tag{16}$$

It can be found that $p(\boldsymbol{\alpha}|a, b)$ obeys the student's T distribution, which can effectively ensure the sparsity of the original signal $\boldsymbol{\alpha}$. According to the same method, the inverse of the noise variance $\sigma_0 = \sigma_n^{-2}$ is processed, and the following expression can be obtained

$$p(\sigma_0|c, d) = \Gamma(\sigma_0|c, d) \tag{17}$$

The prior distribution of parameters $\boldsymbol{\alpha}$ and σ_0 are known. Given the measurement signal $\boldsymbol{y}$ and the observation matrix $\boldsymbol{\Theta}$, the posterior distribution of $\boldsymbol{\alpha}$ can be obtained by Bayesian formula

$$p(\boldsymbol{\alpha}|\boldsymbol{y}, \boldsymbol{\sigma}, \sigma_0) = \frac{p(\boldsymbol{y}|\boldsymbol{\alpha}, \sigma_0)p(\boldsymbol{\alpha}|\boldsymbol{\sigma})}{p(y|\boldsymbol{\sigma}, \sigma_0)} \sim N(\boldsymbol{\mu}, \boldsymbol{\Sigma}) \tag{18}$$

The probability distribution of posterior $\boldsymbol{\alpha}$ in Eq. (18) is a multivariate Gaussian distribution with mean $\boldsymbol{\mu}$ and covariance $\boldsymbol{\Sigma}$. The mean and variance are

$$\boldsymbol{\mu} = \sigma_0 \boldsymbol{\Sigma\Theta}^T \mathbf{y} \tag{19}$$

$$\boldsymbol{\Sigma} = (\sigma_0 \boldsymbol{\Theta}^T \boldsymbol{\Theta} + \mathbf{A})^{-1} \tag{20}$$

$\boldsymbol{A}$ is a diagonal matrix, and its diagonal elements are ($\boldsymbol{\sigma}_1$, $\boldsymbol{\sigma}_2$,...,$\boldsymbol{\sigma}_N$). It is only necessary to estimate the parameters $\boldsymbol{\sigma}$ and $\boldsymbol{\sigma}_0$ to obtain the value of $\boldsymbol{\alpha}$. The logarithm of the edge likelihood function of signal $\boldsymbol{\alpha}$ with respect to parameters $\boldsymbol{\sigma}$ and $\boldsymbol{\sigma}_0$ is

$$\begin{aligned} L(\boldsymbol{\sigma}, \sigma_0) &= \log p\,(\mathbf{y}|\boldsymbol{\sigma}, \sigma_0) \\ &= \frac{1}{2}[M \log 2\pi + \log|\boldsymbol{C}| + \mathbf{y}^T \mathbf{C}^{-1} \mathbf{y}] \end{aligned} \tag{21}$$

In the equation, $\boldsymbol{\sigma} = [\sigma_1, \sigma_2, \ldots, \sigma_N]$, $\mathbf{C} = \sigma_n^{-2}\mathbf{I} + \boldsymbol{\Theta A}^{-1}\boldsymbol{\Theta}^T$. Using the Expectation Maximization (EM) algorithm proposed by Tipping (2001), we can estimate the parameters σ_i and σ_0, to yield

$$\sigma_i^{new} = \frac{1 - \sigma_i \boldsymbol{\Sigma}_{ii}}{\mu_i^2} \tag{22}$$

$$\frac{1}{\sigma_0^{new}} = \frac{\|\mathbf{y} - \boldsymbol{\Theta u}\|_2^2}{M - \sum_i (1 - \sigma_i \boldsymbol{\Sigma}_{ii})} \tag{23}$$

Initialize σ_i and σ_0, substitute (19), (20), (22), (23) for iterative operations, we can obtain mean $\boldsymbol{\mu}$ and covariance $\boldsymbol{\Sigma}$. In order to simplify the calculation, we use the Fast Relevance Vector Machine (FRVM) proposed in Faul and Tipping (2002) to perform iterative calculation. The FRVM can effectively increases the relevant basis functions in the matrix $\boldsymbol{\Theta}$ and deletes the irrelevant basis functions, so that only K relevant basis functions are finally included in the matrix $\boldsymbol{\Theta}$. Finally, we can obtain σ_{iMAP}, σ_{0MAP} and the corresponding signal $\boldsymbol{\alpha}$. It is worth noting that when the sparsity K is small, the calculation amount of matrix inversion in equation (20) is $O(NK^2)$, which is less than that of the conventional CS algorithm. In addition, compared with the conventional CS reconstruction algorithm, BCS considers the noise in the compressed sampling process, so it is more suitable for imaging scenes with noise.

4. BCS-based tomography

For corrosion monitoring of aircraft structures, the damage area is generally only a small fraction of the whole structure to be monitored, so most elements of the slowness changes vector should be zero. That is to say, the vector $\Delta \boldsymbol{S}$ is sparse, that meet the prerequisites of CS.

Then, a measurement matrix can be constructed according to the CS theory to reduce the dimension of the wave travel time difference $\Delta \boldsymbol{T}$. We design a random matrix $\boldsymbol{\Phi}_{m\times M}$ (m < M) that has two characteristics: 1) each row has and only one element is 1, the rest is 0; 2) each column has at most one element of 1, and the rest are 0. The matrix constructed in this way conforms to the Bernoulli distribution, which can satisfy the RIP characteristics and irrelevant conditions in the CS theory. The matrix form is as follows

$$\boldsymbol{\Phi} = \begin{bmatrix} 0 & 0 & \cdots & 0 & 1 \\ 1 & 0 & \cdots & 0 & 0 \\ \vdots & & \ddots & & \vdots \\ 0 & 1 & \cdots & 0 & 0 \end{bmatrix}_{m\times M} \tag{24}$$

Multiply the matrix $\boldsymbol{\Phi}$ and travel time difference $\Delta \boldsymbol{T}$, we can get

$$\boldsymbol{\Delta T}'_{m\times 1} = \Phi_{m\times M} \cdot \Delta T_{M\times 1} = \Phi_{m\times M} \cdot L_{M\times N} \cdot \Delta S_{N\times 1} \tag{25}$$

Through compressed sampling, the wave travel time difference to be measured is reduced from M dimension ($\Delta \boldsymbol{T}$) to m dimension ($\Delta \boldsymbol{T}'$). That is, as long as m paths are randomly selected from M paths, the slowness difference $\Delta \boldsymbol{S}$, which represents the corrosion location, can be reconstructed by CS theory. Thereby the purpose of simplifying the number of sensors in the LWT can be obtained.

BCS is a reconstruction algorithm of CS, which uses Bayesian formula to calculate a posterior estimation of the slowness difference $\Delta \boldsymbol{S}$. After adding the noise, the compressed wave travel time difference can be written

$$\boldsymbol{\Delta T}' = \boldsymbol{\Phi} \cdot \boldsymbol{L} \cdot \boldsymbol{\Delta S} + \boldsymbol{e} = \boldsymbol{\Theta} \cdot \boldsymbol{\Delta S} + \boldsymbol{e} \tag{26}$$

The wave travel time difference $\Delta \boldsymbol{T}'$ is obtained by subtracting the lamb wave travel time under damage condition from the lamb wave travel time under undamaged condition, and its value can be obtained through actual measurement. According to the content of section 2, the distance matrix $\boldsymbol{L}$ can be constructed. The function of the measurement matrix $\boldsymbol{\Phi}$ is to randomly select m rows from the distance matrix $\boldsymbol{L}$. $\boldsymbol{e}$ is Gaussian noise with a mean value of zero and a variance of σ_n^2. Therefore, the probability distribution function of $\Delta \boldsymbol{S}$ can be estimated by BCS reconstruction algorithm introduced in section 3. The nonzero element in the $\Delta \boldsymbol{S}$ corresponds to the location where corrosion occurs. Fig. 2 shows the corrosion monitoring implementation process using BCS-based tomography method.

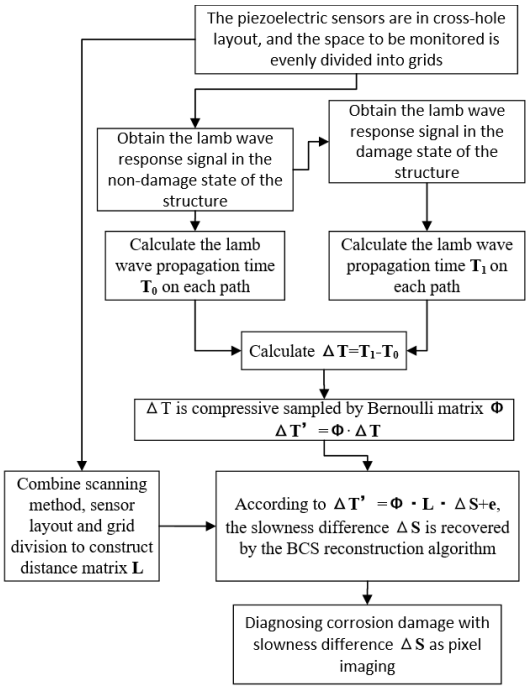

Fig. 2 Schematic diagram of the corrosion monitoring using BCS-based tomography

5. Numerical simulation

5.1 Corrosion localization simulation without noise

We performed corrosion localization simulation on an aviation aluminum plate with a thickness of 0.3cm and a monitoring area of 20 cm × 20 cm. The computer used for simulation has an inter i5 dual CPU with frequency of 1.6 GHz, 1.8 GHz and a memory of 8G. Chang *et al*. (2020) obtains the conclusion that when the number of sensors is no less than 15 pairs, the CS reconstruction success rate can reach 100%. Therefore, we use 15 pairs of sensors to locate the corrosion.

In order to verify the localization effect of the methods at different positions, corrosion is placed at coordinates (7 cm, 8 cm) and (13 cm, 12 cm) of the monitoring area, where is called corrosion 1 and corrosion 2, as shown in Fig. 3. First, the monitoring area is discretized and divided into 40 × 40 equidistant grids, 15 pairs of sensors are arranged on both sides. Fig. 4 shows the sensors layout, ray distribution and corrosion position in the simulation. The yellow grid area in the figure represents the location where corrosion occurs.

According to the dispersion characteristics of lamb wave, the velocity of lamb wave in undamaged state (thickness 0.3 cm) is obtained and travel time vector $\mathbf{T}_0$ is calculated. Assuming that the thickness of the corrosion location is 0.2 cm, travel time vector $\mathbf{T}_1$ under the corrosion condition is calculated, and the travel time difference signal $\Delta \boldsymbol{T}'$ can be obtained. According to the method described in Section 2, the distance matrix $\mathbf{L}$ can be obtained.

We used LWT method, CS-based tomography method and BCS-based tomography method respectively to locate corrosion 1 and corrosion 2 in the absence of noise. Fig. 5

(a) Corrosion 1 (b) Corrosion 2

Fig. 3 Schematic diagram of monitoring area and corrosion location

(a) Corrosion 1 (b) Corrosion 2

Fig. 4 Sensor layout, ray distribution and corrosion position in the simulation

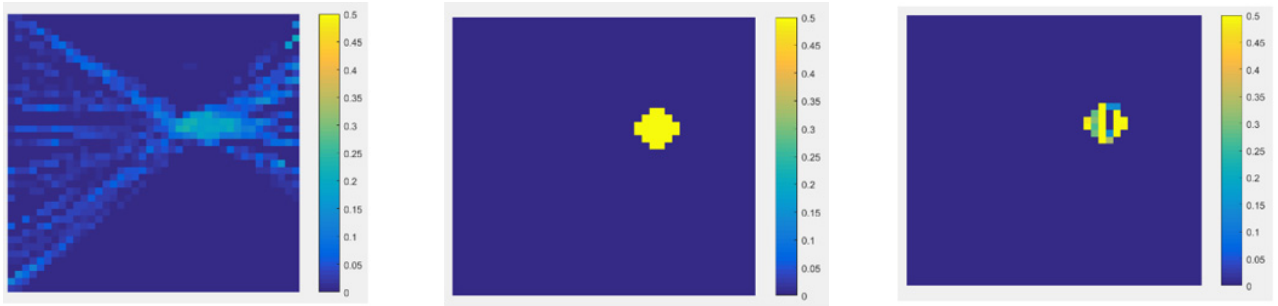

(a) Image by LWT method (b) Image by CS-based tomography method (c) Image by BCS-based tomography method

Fig. 5 Simulation imaging results of corrosion 1 without noise

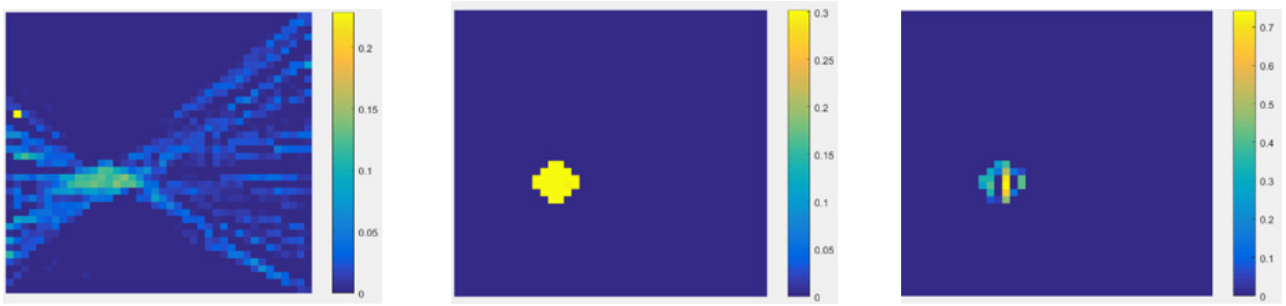

(a) Image by LWT method (b) Image by CS-based tomography method (c) Image by BCS-based tomography method

Fig. 6 Simulation imaging results of corrosion 2 without noise

shows the simulation imaging results of corrosion 1 by the three methods. And Fig. 6 shows the simulation imaging results of corrosion 2 by the three methods.

From Fig. 5 and Fig. 6, the center coordinates of grids in which the pixels are significantly higher than the undamaged portion are found, and the average values of the horizontal and vertical coordinates are calculated, thereby the coordinates of the damage center position can be obtained. Table 1 summarizes the localization results, localization errors and running time of those three methods.

Table 1 Localization results of corrosion simulation without noise

	LWT method			CS-based tomography method			BCS-based tomography method		
	Localization results (cm)	Error (cm)	Running time (s)	Localization results (cm)	Error (cm)	Running time (s)	Localization results (cm)	Error (cm)	Running time (s)
Corrosion 1	(9.82,10.95)	3.35	2.248	(13.00,12.00)	0	1.961	(12.95,12.00)	0.05	0.204
Corrosion 2	(9.51,9.95)	3.18	2.171	(7.00,8.00)	0	1.692	(6.96,7.95)	0.06	0.183

From the results, LWT method cannot clearly image the corrosions, and its localization error is big. Both CS-based tomography and BCS-based tomography can accurately locate the corrosions and display the corrosions shape. Actually, the entire monitoring area is basically covered by rays under 15 pairs of sensors, so corrosion can be accurately located anywhere within the monitoring area by the both methods. In terms of imaging speed, LWT has the longest imaging time, the BCS-based tomography has the shortest imaging time, and BCS-based tomography is significantly faster than CS-based tomography.

5.2 corrosion localization simulation with noise

In actual environment, the measurement signal often contains noise. Therefore, for corrosion1 we add Gaussian noise with SNR of 10, 20, 30, 40 to the measured signal $\Delta \boldsymbol{T}$, and then use the three methods to reconstruct the slowness difference $\Delta \boldsymbol{S}$ to achieve the location of corrosion respectively.

Figs. 7, 8, 9, 10 show the corrosion images obtained by the three reconstruction methods under different SNR. Table 2 summarizes the localization results, localization errors and running time of those three methods with different SNR. According to the simulation results, the LWT has poor imaging effect, it is difficult to accurately display the corrosion location and sharp, and it takes the longest time. The image of CS-based tomography has artifacts, and the artifacts which affect imaging effect increase gradually as the SNR decreases. In addition, CS-based tomography has a long running time. Compare with the two imaging methods, the new proposed BCS-based tomography is less affected by noise, has better image quality, fewer artifacts, can accurately display the location and shape of corrosion, and has the shortest imaging time.

Through the simulation, we can obtain the following conclusion: Although the image quality of BCS-based tomography is slightly inferior to CS-based tomography in the absence of noise, it does not affect the display of corrosion shape and position. Further, BCS-based tomography has fewer artifacts and faster localization speed than CS-based tomography in noisy environments. There is noise in practical engineering application, so the BCS-based tomography has a greater application prospect.

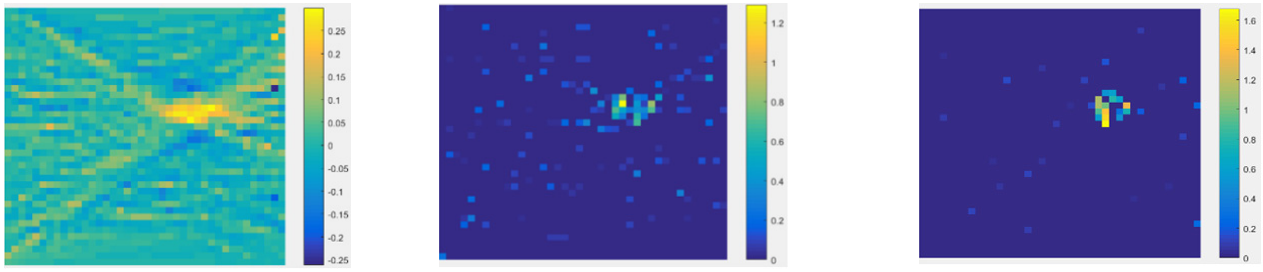

(a) Image by LWT method (b) Image by CS-based tomography method (c) Image by BCS-based tomography method

Fig. 7 Simulation imaging results under the SNR is 10

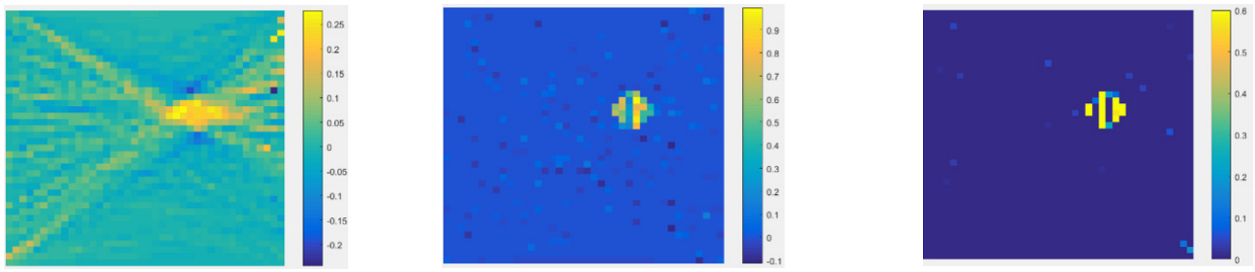

(a) Image by LWT method (b) Image by CS-based tomography method (c) Image by BCS-based tomography method

Fig. 8 Simulation imaging results under the SNR is 20

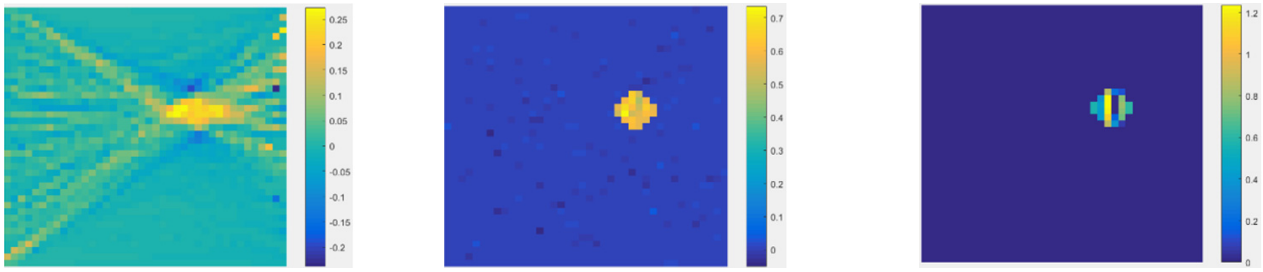

(a) Image by LWT method (b) Image by CS-based tomography method (c) Image by BCS-based tomography method

Fig. 9 Simulation imaging results under the SNR is 30

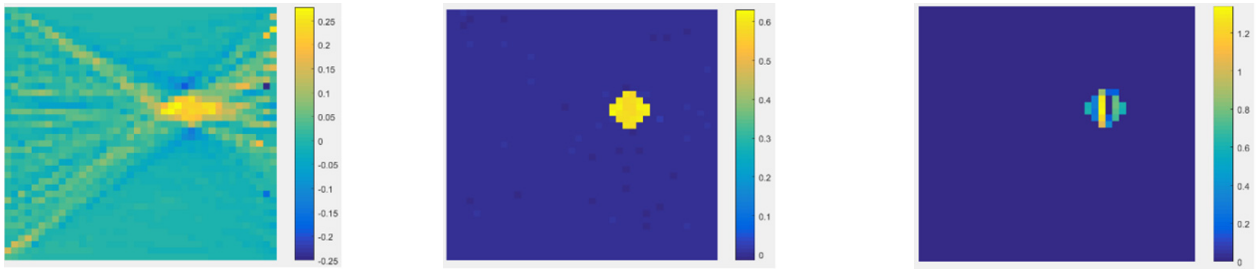

(a) Image by LWT method (b) Image by CS-based tomography method (c) Image by BCS-based tomography method

Fig. 10 Simulation imaging results under the SNR is 40

Table 2 localization results of corrosion simulation with noise

SNR	LWT method			CS-based tomography method			BCS-based tomography method		
	Localization results (cm)	Error (cm)	Running time (s)	Localization results (cm)	Error (cm)	Running time (s)	Localization results (cm)	Error (cm)	Running time (s)
10	inapplicability	—	2.815	(11.52,11.01)	1.74	2.216	(12.84, 11.79)	0.26	0.591
20	inapplicability	—	2.615	(12.08,11.50)	1.05	2.176	(12.89, 11.90)	0.15	0.448
30	inapplicability	—	2.819	(12.81,11.82)	0.26	2.463	(12.94, 12.00)	0.06	0.175
40	inapplicability	—	2.716	(12.97,11.95)	0.06	2.519	(12.93, 12.00)	0.06	0.180

6. Experimental verification

6.1 Experimental setup

According to simulation analysis, we use a square 2024 aviation aluminum alloy with a thickness of 0.3 cm and an overall structure of 50 cm in length for verification experiments. 15 pairs of piezoelectric sensors are arranged on both sides of the monitoring area to monitor the area of 200 mm × 200 mm in the aluminum plate. The corrosion point with a diameter of 3cm is artificially manufactured in the upper right corner of the monitoring area. The schematic diagram of the experimental monitoring area and the corrosion position is shown in Fig. 11. Experiment uses multi-channel scanning system developed by author's research group to generate excitation signals and receive signals. The instruments and specimen used in the experiment are shown in Fig. 12. The multi-channel scanning system has a dual CPU with frequency of 2.2 GHz, 1.8 GHz. a memory of 8 G.

6.2 Experimental signal

The propagation of lamb waves in aluminum plates is complicated, which reflect the characteristics of dispersion. In addition, the lamb wave of each frequency contains symmetric and antisymmetric modes, so the final lamb wave sensing signal that can be obtained will reflect the result of dispersion and multi-mode superposition. In this experiment, a 0.3 cm thick 2024 aviation aluminum plate was selected. According to the parameters of the aluminum plate, the dispersion curve of the group velocity of each mode lamb wave in the aluminum plate with the frequency-thickness product was calculated, as shown in Fig. 13.

It can be seen from the figure that in the range where the frequency-thickness product is less than 600 KHz·mm, only the A_0 mode and S_0 mode exist. In this range, the group velocity of the A_0 mode and the S_0 mode are quite different, so it is easy to distinguish and extract the two modes. Moreover, the group velocity of mode A_0 is more sensitive to the change of plate thickness, which is conducive to the identification of defects. Therefore, the center frequency of

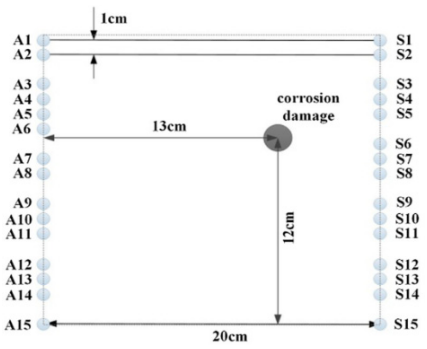

Fig. 11 Schematic diagram of experimental monitoring area, sensor layout and corrosion

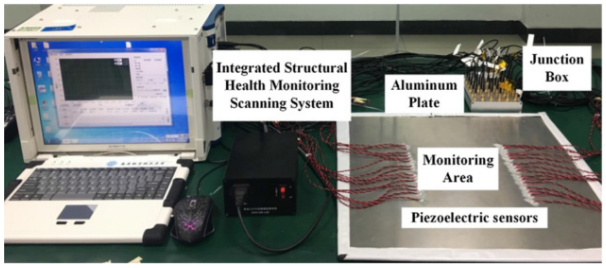

Fig. 12 Instruments in the monitoring experiment

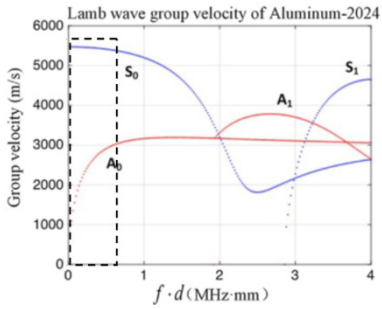

Fig. 13 Dispersion curve of lamb wave in aluminum plate

excitation signal in this experiment is chose to be 60 kHz, and the lamb wave arrival time is determined by the travel time of the group velocity of the A_0 mode at 60 kHz.

6.3 Calculation of lamb wave arrival time

The excitation signal selected in this experiment is a five-cycle-modified sine wave with a center frequency of 60 kHz. The sampling frequency is set to 10 M/s, and the sampling length is 5000 data points.

An adaptive threshold method is used to extract the lamb wave travel time. The threshold value is the product of adaptive coefficient c and the amplitude of the secondary peak V_p, that is $c \cdot V_p$. The threshold value $c \cdot V_p$ is required to be greater than the peak amplitude before the secondary peak. In this experiment, the value of coefficient c is 0.6, that is mean that the starting point is 60% of the secondary peak in rise stage of the excitation signal, and the end point is 60% of the secondary peak in rise stage of the sensing signal. The time difference between the two points is the

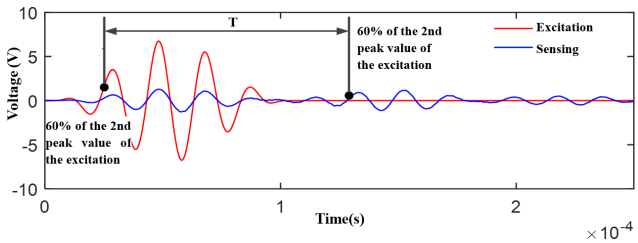

Fig. 14 Schematic diagram of calculation of lamb wave arrival time

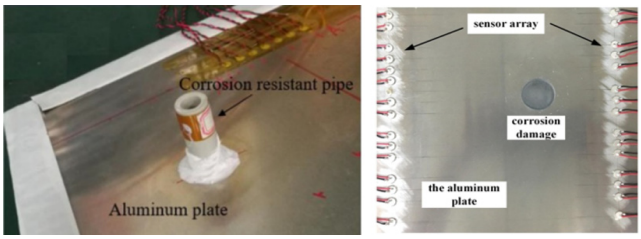

Fig. 15 Aluminum plate during and after corrosion

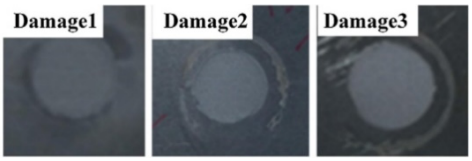

Fig. 16 Three different severity of corrosion damage

required travel time $\boldsymbol{T}$. Fig. 14 is a schematic diagram of the excitation signal, the sensing signal and the adaptive threshold method.

6.4 Experimental process

First, under the condition of no damage, 225(15×15) excitation sensing routes are generated, and the travel time $\boldsymbol{T}_0$ of the lamb wave under the condition of no damage is calculated. Next, artificial corrosion is produced. Here, corrosion is produced by a chemical reaction between a hydrochloric acid solution and metal aluminum. we use glass glue to fix the 3 cm diameter Polypropylene-Random (PPR) tube at the position to be corroded on the aluminum plate. After the glass glue is cured, hydrochloric acid is added to the tube, and the hydrochloric acid reacts with the aluminum plate for corrosion. Fig. 15 shows the aluminum plate during and after corrosion. After the corrosion is made, the PACSCAN ultrasonic c-scan is used to measure the corrosion depth. In this experiment, the same position on the aluminum plate was corroded three times, and three corrosion damages with different corrosion depths were formed at different stages, marked as “Damage 1”, “Damage 2”, and “Damage 3”, as shown in Fig. 16. The depths of the three corrosions measured by the ultrasonic c-scan system are 0.011 cm, 0.041 cm and 0.059 cm, respectively.

We can obtain $\boldsymbol{T}_{corrosion1}$, $\boldsymbol{T}_{corrosion2}$, and $\boldsymbol{T}_{corrosion3}$ by measure the travel time of the A_0 mode of lamb wave in

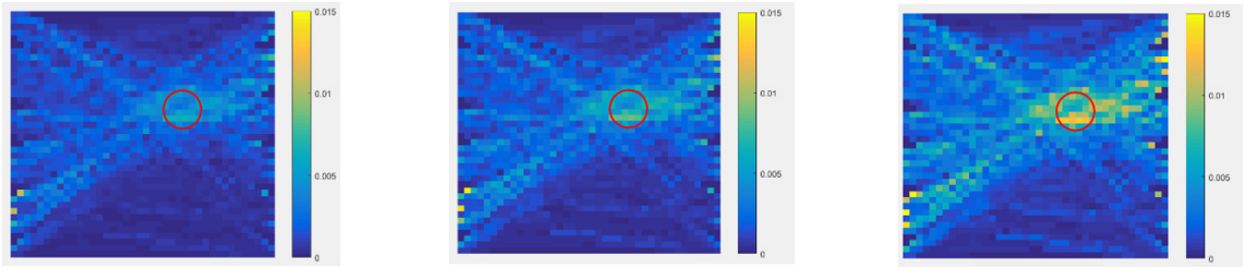

(a) Reconstructed image of Damage 1 (b) Reconstructed image of Damage 2 (c) Reconstructed image of Damage 3

Fig. 17 Corrosion damage imaging by LWT method

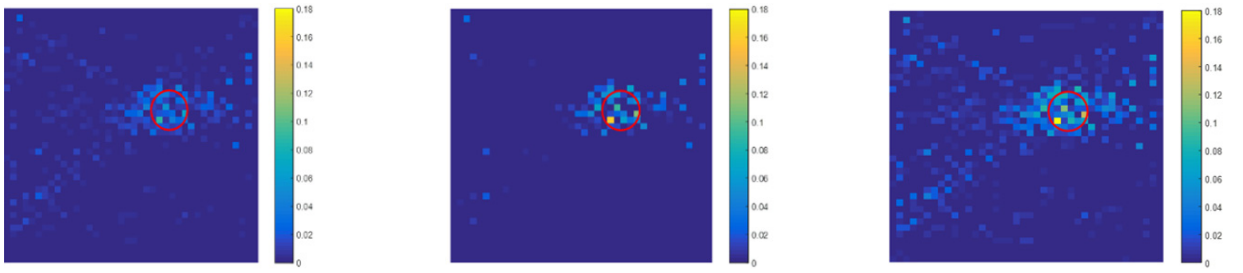

(a) Reconstructed image of Damage 1 (b) Reconstructed image of Damage 2 (c) Reconstructed image of Damage 3

Fig. 18 Corrosion damage imaging by CS-based tomography method

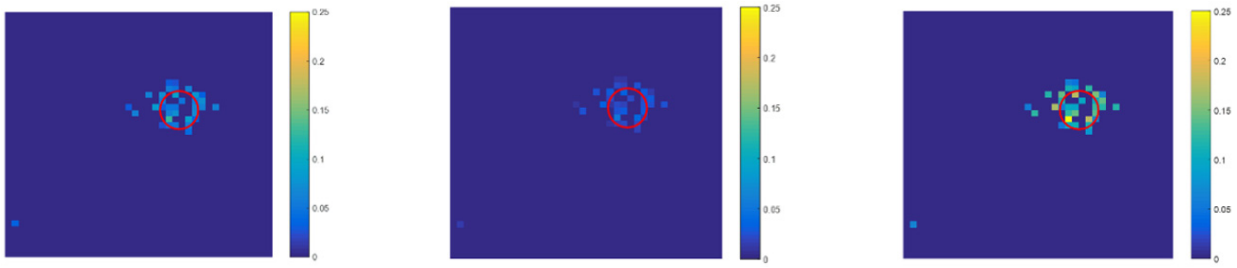

(a) Reconstructed image of Damage 1 (b) Reconstructed image of Damage 2 (c) Reconstructed image of Damage 3

Fig. 19 Corrosion damage imaging by BCS-based tomography method

different corrosion stages. Using these data to subtract the travel time $\boldsymbol{T}_0$ of the lamb wave A_0 mode in non-damage environment, the travel time difference vector $\Delta\boldsymbol{T}_1'$, $\Delta\boldsymbol{T}_2'$ and $\Delta\boldsymbol{T}_3'$ can be obtained. Substituting the travel time difference $\Delta\boldsymbol{T}'$, measurement matrix $\boldsymbol{\Phi}$ and distance matrix $\boldsymbol{L}$ into Eq. (26), and the slowness difference $\Delta\boldsymbol{S}$ is obtained by BCS reconstructing algorithm, whose nonzero elements represent where the corrosion occurs.

6.5 Results and discussion

6.5.1 Experimental results

LWT, CS-based tomography and BCS-based tomography are used to localize the corrosion at those three different corrosion stages of aluminum plates respectively. Figs. 17, 18 and 19 are the corrosion imaging results of the three reconstruction methods. The red circle in those figures are the actual location and shape of corrosion. Among the three methods, the imaging results of LWT method are

Table 3 Localization results with real corrosion location of (13.00 cm, 12.00 cm)

	LWT method			CS-based tomography method			BCS-based tomography method		
	Localization results (cm)	Error (cm)	Running time (s)	Localization results (cm)	Error (cm)	Running time (s)	Localization results (cm)	Error (cm)	Running time (s)
Damage 1	inapplicability	—	2.975	(12.10,11.49)	1.03	2.437	(12.90,12.13)	0.16	0.432
Damage 2	inapplicability	—	3.024	(12.28,11.54)	0.85	2.501	(12.89,12.13)	0.17	0.511
Damage 3	inapplicability	—	3.105	(12.04,11.42)	1.12	2.615	(12.89,12.13)	0.17	0.623

relatively fuzzy, the location and shape of the corrosion cannot be accurately located. CS-based tomography method can monitor the corrosion from location, shape and depth, but the imaging effect is not good which have many artifacts. BCS-based tomography method can monitor the corrosion from location, shape and depth, and the imaging result have fewer artifacts that make the images have higher recognition. Table 3 shows the corrosion positioning results and the running time of the three methods. According to the experimental results, BCS-based tomography method has the best localization effect and the shortest localization time.

6.5.2 Discussion

BCS-based tomography method can achieve accurate corrosion localization with fewer sensors, and the corrosion imaging has fewer artifacts and shorter imaging time. These make the BCS-based tomographic method more advantageous than the traditional LWT method and CS-based tomographic method in aircraft corrosion structure monitoring.

Although BCS-based tomographic method has many advantages, it is important to note that the new method is performed under the premise that the ambient noise obeys Gaussian distribution. The aircraft flight environment is complex and changeable. Although most of the noise is Gaussian noise, it may be accompanied by other forms of uncertain noise for a certain period of time, which will affect the diagnosis of the new method. Therefore, when using BCS-based tomography method for aircraft structural corrosion monitoring, it is necessary to make multiple measurements at certain interval.

7. Conclusions

In order to optimize the existing LWT method, on the basis of CS-based tomographic, this paper proposes a BCS-based tomographic method for aircraft structural corrosion monitoring. The new proposed method uses Bayesian compressive sensing to position the corrosion of structure, which reduces the number of sensors and the image artifacts. Both simulation and experimental study on the method are carried out. The result shows that the new method can locate corrosion and diagnose the different corrosion depths of aluminum plate. Furthermore, the imaging quality and imaging time of the new method are improved compared with the traditional LWT and CS-based tomographic, which are conducive to the corrosion monitoring of aircraft structures.

Acknowledgments

This work is supported by the Fundamental Research Funds for the Central Universities [grant number NI2023001], the Fund of Prospective Layout of Scientific Research for Nanjing University of Aeronautics and Astronautics, the Research Fund of State Key Laboratory of Mechanics and Control for Aerospace Structures (Nanjing University of Aeronautics and astronautics) [grant number MCAS-I-0423G01] and the Priority Academic Program Development of Jiangsu Higher Education Institutions of China.

References

Alexopoulos, N.D., Dalakouras, C.J., Skarvelis, P. and Kourkoulis, S.K. (2012), "Accelerated corrosion exposure in ultra thin sheets of 2024 aircraft aluminum alloy for GLARE applications", *Corros. Sci.*, **55**(2), 289-300. https://doi.org/10.1016/j.corsci.2011.10.032

Bao, Q., Yuan, S., Guo, F. and Qiu, L. (2019), "Transmitter beamforming and weighted image fusion-based multiple signal classification algorithm for corrosion monitoring", *Struct. Health Monitor.*, **18**(2), 621-634. https://doi.org/10.1177/1475921718764848

Baraniuk, R. (2007), "A lecture on compressive sensing", *IEEE Signal Processing Magazine*, **24**(4), 1-9. https://doi.org/10.1109/MSP.2007.4286571

Belanger, P. (2010), "Feasibility of Thickness Mapping Using Ultrasonic Guided Waves", Ph.D. Dissertation; Imperial college London, London, UK.

Braga, D.F., Tavares, S.M.O., Silva, L.F., Moreira, P.M.G.P. and De Castro, P.M. (2014), "Advanced design for lightweight structures: Review and prospects", *Progress Aerosp. Sci.*, **69**, 29-39. https://doi.org/10.1016/j.paerosci.2014.03.003

Candes, E.J., Romberg, J.K. and Tao, T. (2006), "Stable signal recovery from incomplete and inaccurate measurements", *Commun. Pure Appl. Mathe.*, **59**(8), 1207-1223. https://doi.org/10.1002/cpa.20124

Chang, M., Yuan, S. and Guo, F. (2020), "Corrosion monitoring using a new compressed sensing-based tomographic method", *Ultrasonics*, **101**(1), 105988. https://doi.org/10.1016/j.ultras.2019.105988

Cirtautas, D., Samaitis, V., Mažeika, L., Raišutis, R. and Žukauskas, E. (2022), "Selection of higher order lamb wave mode for assessment of pipeline corrosion", *Metals*, **12**(3), 503. https://doi.org/10.3390/met12030503

Donoho, D.L. (2006), "Compressed sensing", *IEEE Trans. Inform. Theory*, **52**(4), 1289-1306. https://doi.org/10.1109/TIT.2006.871582

Faul, A.C. and Tipping, M.E. (2002), "Analysis of sparse Bayesian learning", In: *International Conference on Nerual Information Processing Systems*; *Natural & Syntheic*, Boston, USA, January.

Garg, M., Sharma, S., Sharma, S. and Mehta, R. (2016), "Non-contact damage monitoring technique for FRP laminates using guided waves", *Smart Struct. Syst., Int. J.*, **17**(5), 795-817. https://doi.org/10.12989/sss.2016.17.5.795

Gorgin, R. and Wang, Z. (2021), "Baseline-free damage imaging technique for Lamb wave based structural health monitoring systems", *Smart Struct. Syst., Int. J.*, **28**(5), 689-698. https://doi.org/10.12989/sss.2021.28.5.689

He, J., Gao, R. and Zhou, H. (2023), "A nonparametric seismic reliability analysis method based on Bayesian compressive sensing-stochastic harmonic function method and probability density evolution method", *Mech. Syst. Signal Process.*, **196**, 110339. https://doi.org/10.1016/j.ymssp.2023.110339

Huang, S., Yu, Z. and Shen, W. (2016), "Multi-mode electromagnetic ultrasonic lamb wave tomography imaging for variable-depth defects in metal plates", *Sensors*, **16**(5), 628. https://doi.org/10.3390/s160506 28

Huang, L., Ding, J., Lin, J. and Luo, Z. (2024), "Detection and localization of corrosion using identical-group-velocity Lamb wave modes", *Nondestr. Test. Eval.*, **39**(3), 594-613. https://doi.org/10.1080/10589759.2023.2218007

Ji, S., Xue, Y. and Carin, L. (2008), "Bayesian Compressive

Sensing", *IEEE Transact. Signal Process.*, **56**(6), 2346-2356. https://doi.org/10.1109/TSP.2007.914345

Kullaa, J. (2021), "Damage detection and localization under variable environmental conditions using compressed and reconstructed bayesian virtual sensor data", *Sensors*, **22**(1), 306. https://doi.org/10.3390/s22010306

Livadiotis, S., Sitaropoulos, K., Ebrahimkhanlou, A. and Salamone, S. (2023), "Acoustic emission monitoring of corrosion in steel pipes using Lamb-type helical waves", *Struct. Health Monitor.*, **22**(2), 1225-1236. https://doi.org/10.1177/14759217221105644

Salucci, M., Anselmi, N., Migliore, M.D. and Massa, A. (2022), "A Bayesian compressive sensing approach to robust near-field antenna characterization", *IEEE Transact. Antennas Propag.*, **70**(9), 8671-8676. https://doi.org/10.1109/TAP.2022.3177528

Tipping, M.E. (2001), "Sparse Bayesian learning and the relevance vector machine", *J. Mach. Learn. Res.*, **1**(3), 211-244. https://doi.org/10.1162/15324430152748236

Tsaig, Y. and Donoho, D.L. (2006), "Extensions of compressed sensing", *Signal Process.*, **86**(3), 549-571. https://dou.org/10.1016/j.sigpro.2005.05.029

Vivar-Perez, J.M., Duczek, S. and Gabbert, U. (2014), "Analytical and higher order finite element hybrid approach for an efficient simulation of ultrasonic guided waves I: 2D-analysis", *Smart Struct. Syst., Int. J.*, **13**(4), 587-614. https://doi.org/10.12989/sss.2014.13.4.587

Xiao, Y., Yuan, L., Liu, Y., Wang, J., Hu, W., Sun, R. and Ni, P. (2024), "Sparse reconstruction of sound field using pattern-coupled Bayesian compressive sensing", *J. Acoust. Soc. Am.*, **156**(1), 548-559. https://doi.org/10.1121/10.0027933

Xu, J., Pi, Y. and Cao, Z. (2012), "Bayesian compressive sensing in synthetic aperture radar imaging", *IET Radar Sonar Navig.*, **6**(1), 2-8. https://doi.org/10.1049/iet-rsn.2010.0375

Zhao, X., Royer, R.L., Owens, S.E. and Rose, J.L. (2011), "Ultrasonic Lamb wave tomography in structural health monitoring", *Smart Mater. Struct.*, **20**(10), 105002. https://doi.org/10.1088/0964-1726/20/10/105002

Zima, B., Woloszyk, K. and Garbatov, Y. (2022), "Experimental and numerical identification of corrosion degradation of ageing structural components", *Ocean Eng.*, **258**, 111739. https://doi.org/10.1016/j.oceaneng.2022.111739